

# Synergy of Ru and Ir in the Electrohydrogenation of Toluene to Methylcyclohexane on a Ketjenblack-Supported Ru-Ir Alloy Cathode

Yuta Inami,<sup>†</sup> Hitoshi Ogihara,<sup>†</sup> Shinichi Nagamatsu,<sup>‡</sup> Kiyotaka Asakura,<sup>‡</sup> and Ichiro Yamanaka<sup>\*,†</sup>

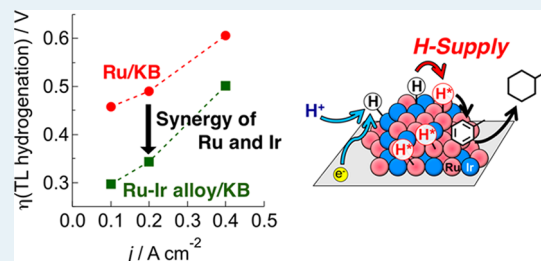
<sup>†</sup>Department of Chemical Science and Engineering, School of Materials and Chemical Technology, Tokyo Institute of Technology, Tokyo, 152-8552, Japan

<sup>‡</sup>Institute for Catalysis, Hokkaido University, Hokkaido 001-0021, Japan

## Supporting Information

**ABSTRACT:** An organic hydride system based on hydrogenation/dehydrogenation of toluene (TL)/methylcyclohexane (MCH) has been studied as a hydrogen storage technology. Electrohydrogenation of TL to MCH using a proton exchange membrane (PEM) electrolyzer is proposed as a candidate for the hydrogenation of TL in the organic hydride system. Recently, we reported that a Ketjenblack-supported Ru-Ir alloy (Ru-Ir/KB) cathode was effective for the reaction; however, electrohydrogenation mechanisms and catalyses of Ru and Ir in the electrohydrogenation have been unclear. In this paper, detailed characterization studies using transmission electron microscopy (TEM) with energy-dispersive X-ray spectroscopy (EDS), X-ray diffraction (XRD), X-ray absorption fine structure (XAFS), X-ray photoelectron spectroscopy (XPS), and electrochemical studies using cyclic voltammetry (CV) and linear sweep voltammetry (LSV) for hydrogen evolution and kinetic studies for catalytic hydrogenation of TL by Ru-Ir/KB catalysts were conducted. On the basis of the experimental results, the electrohydrogenation mechanisms and synergy of Ru and Ir were proposed.

**KEYWORDS:** electrohydrogenation, Ru and Ir synergy, spillover, PEM electrolyzer

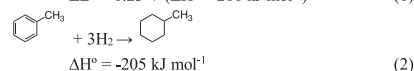
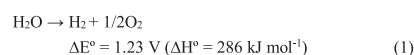


## INTRODUCTION

Hydrogen energy has attracted attention as an alternative energy source to fossil fuels. If hydrogen is produced from water and renewable energy, hydrogen will be the ultimate clean secondary energy. One of the most critical obstacles for practical utilization of hydrogen energy is the difficulty in storage and transportation of gaseous  $\text{H}_2$ .<sup>1</sup> A high-pressure technology of  $\text{H}_2$  is well-established; however, the technology is not appropriate for large-scale storage and long-term transportation of  $\text{H}_2$ , because of a low volumetric mass density ( $39 \text{ kg of } \text{H}_2 \text{ m}^{-3}$ ) even at very high pressure (70 MPa) and a high volatility. In addition, the handling of gaseous  $\text{H}_2$  is not easy because it is an explosive and leaky gas. Therefore, candidate technologies, such as cryogenic liquid hydrogen, liquid ammonia, absorption in metal compounds, and liquid organic hydrides are proposed for hydrogen storage and transportation.<sup>1</sup>

The organic hydride technology is based on the hydrogenation/dehydrogenation of organic compounds couple.<sup>2–4</sup> It is considered that the toluene (TL)/methylcyclohexane (MCH) couple is the most suitable for large-scale storage for the following reasons.<sup>5</sup> (i) Handling of TL and MCH is easy because their toxicities are not too high and they are stable as liquids under ambient conditions. (ii) The volumetric mass density is fairly high ( $47.4 \text{ kg of } \text{H}_2 \text{ m}^{-3}$ ). (iii) The current petroleum infrastructure can be used. (iv) A large amount of TL is available from petroleum resources. Though an industrial

process for the catalytic dehydrogenation of MCH to TL using a  $\text{Pt}/\text{Al}_2\text{O}_3$ -based catalyst has been developed,<sup>3,5</sup> there is room for improvement for the hydrogenation process. As mentioned before, a catalytic process for hydrogenation of TL to MCH was proposed as shown below.<sup>3,5</sup> The first step is water electrolysis using renewable energy to produce  $\text{H}_2$  (eq 1), and



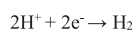
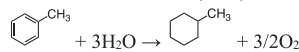
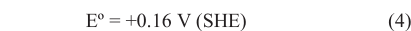
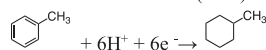
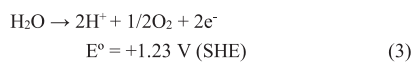
the second step is the catalytic hydrogenation of TL at higher temperature and under pressure conditions (eq 2), though the second step is an exothermic reaction. We cannot avoid a heat loss in the hydrogenation process, because a perfect heat recovery cannot be achieved in the chemical process.

If MCH could be directly produced from TL and water by an electrochemical method, we would avoid the heat loss in eq 2. In other words, the efficiency of energy conversion defined as a quantity of MCH production against the energy consumption would increase in the direct production process. Thus, electrohydrogenation of TL to MCH coupled with

Received: September 7, 2018

Revised: January 8, 2019

electro-oxidation of water using a proton exchange membrane (PEM) electrolysis cell<sup>6,7</sup> is proposed.<sup>8–10</sup> In the system, water is oxidized to oxygen, protons, and electrons on an anode (eq 3) and TL is reduced with protons and electrons to MCH on a



cathode (eq 4). The total reaction is indicated in eq 5. The theoretical electrolysis voltage of the reaction is 1.07 V, which is smaller than the 1.23 V for the water electrolysis (eq 1). The efficiency of energy conversion for the MCH production would increase by using the electrohydrogenation system. In addition, the electrochemical formation of H<sub>2</sub> (eq 6) is a competitive reaction with the MCH formation. To achieve an efficient electrohydrogenation of TL to MCH, selective and active electrocatalysis of the cathode is essential. Suppression of the hydrogen formation is the key technology.

It has been reported that cathodes with a high loading of Pt (50 wt %) supported on carbon (Pt/C) and a high loading of Pt-Ru alloy (54 wt %) supported on carbon (Pt-Ru/C) are effective for the selective electrohydrogenation of TL to MCH.<sup>9,11</sup> However, studies focusing on non-Pt cathodes are very limited.<sup>12–14</sup> Recently, we widely evaluated the electrohydrogenation activities of carbon-supported precious-metal cathodes and reported that Ru/Ketjenblack (KB) and Rh/KB cathodes showed good Faradaic efficiencies of MCH formation (FEs(MCH)) even at low metal loadings. The Ru/KB cathode was especially active at a lower loading of Ru, but a drawback is the large overpotential for the electrohydrogenation of TL to MCH.<sup>13,14</sup> Furthermore, we have found that the overpotential for the electrohydrogenation of TL drastically decreased by addition of Ir to Ru/KB.<sup>13</sup> In the case of a 5 wt % Ru–5 wt % Ir/KB cathode (0.20 mg<sub>metal</sub> cm<sup>-2</sup>), it showed superior performance for the electrohydrogenation in comparison to the 50 wt % Pt/KB cathode (1.0 mg<sub>Pt</sub> cm<sup>-2</sup>) under galvanostatic electrolysis of 0.20 A cm<sup>-2</sup>. A brief reaction mechanism of the electrohydrogenation of TL to MCH was proposed as (i) adsorbed hydrogen species (H<sub>ad</sub>) formed on the metal surface by the electrochemical reduction of H<sup>+</sup> and (ii) H<sub>ad</sub> on the metals attacked TL adsorbed on metals to form MCH. A strong synergy of Ru and Ir was observed; however, the synergy mechanism for the electrohydrogenation of TL has not been clear.

The purposes of this paper are to identify the active site of the Ru-Ir/KB electrocatalyst by detailed characterization studies and to clarify the synergy mechanism of the electrohydrogenation by Ru and Ir on KB by voltammetric studies and kinetic studies for the catalytic hydrogenation of TL.

## EXPERIMENTAL SECTION

All reagents used in this work are listed in the Supporting Information.

**Preparation of Electrocatalysts.** Ru/KB, Ir/KB, and Ru-Ir/KB electrocatalysts were prepared by chemical reduction using NaBH<sub>4</sub>. The KB powder (90 mg) and deionized water (100 mL) were mixed in a 200 mL PTFE beaker with vigorous stirring. To disperse KB in deionized water, ultrasonication was performed by using an ultrasonic homogenizer (UD-200, TOMY SEIKO Co, Ltd.). Certain amounts of 20 mM RuCl<sub>3</sub>·*n*H<sub>2</sub>O aqueous solutions and 13 mM IrCl<sub>3</sub>·*n*H<sub>2</sub>O aqueous solutions were added to the KB dispersion, and the mixture was heated to 353 K in a bead bath with stirring by a magnetic stirrer. After the mixture was stirred at 353 K for 1 h, NaOH aqueous solutions were added to adjust the pH to 12. NaBH<sub>4</sub> (10 equiv against the amount of total metal) dissolved in NaOH aqueous solution (pH 12, 20 mL) was added dropwise. After overnight stirring, the mixture was filtered, washed with deionized water (100 mL) and 2-propanol (20 mL), and dried under vacuum at 343 K for 1 h. The obtained powders are denoted as Ru(*x*)-Ir(*y*)/KB electrocatalysts, where *x* and *y* are the Ru and Ir loadings (wt %), respectively. The total metal loadings (*x* + *y*) were fixed to 10 wt % for all cathode electrocatalysts prepared in this study.

A 50 wt % Pt/KB electrocatalyst for anode was prepared by the conventional impregnation method. Briefly, 0.1 M H<sub>2</sub>PtCl<sub>6</sub> aqueous solutions were impregnated to KB and dried. The obtained powder was reduced with H<sub>2</sub> at 573 K for 2 h.

**Fabrication of Electrode and Membrane–Electrode Assembly (MEA).** An electrocatalyst ink was prepared by mixing 4.0 mg of the electrocatalyst, 20 μL of 10 wt % Nafion dispersion, and 250 μL of acetone and ultrasonicated for 10 min. The entire ink was cast on GDL (SIGRACET GDL-25BC, 2.0 cm<sup>2</sup>). Subsequently, the electrocatalyst/GDL was dried under vacuum at 323 K for 10 min. The electrocatalyst/GDL was used as a cathode. The catalyst loading was 2.0 mg<sub>catal</sub> cm<sup>-2</sup>, which corresponds to a total metal loading of 0.20 mg<sub>metal</sub> cm<sup>-2</sup>. A 50 wt % Pt/KB/GDL anode (5.0 mg<sub>catal</sub> cm<sup>-2</sup>) was prepared by a similar method. A Nafion117 membrane was sandwiched by the cathode and anode and hot-pressed for 1 min at 50 MPa and 413 K. The MEA electrocatalyst/GDL Nafion117/Pt/KB/GDL was fabricated.

**Electrohydrogenation of TL to MCH.** The MEA was set in a batch type two-compartment electrolysis cell.<sup>13,14</sup> Pure TL (25 mL) was added to the cathode compartment and stirred using a magnetic stir bar. Ar (101 kPa, 20 mL min<sup>-1</sup>) was bubbled into TL solution. Deionized water (15 mL) was added to the anode compartment to humidify the Nafion membrane, and H<sub>2</sub> (101 kPa, 20 mL min<sup>-1</sup>) was flowed as a H<sup>+</sup> source. Hydrogen oxidation proceeded at the anode. A reference electrode of Ag/AgCl saturated KCl (+0.199 V vs standard hydrogen electrode (SHE)) was connected to the Nafion membrane via a 1 M H<sub>2</sub>SO<sub>4</sub> aqueous solution. After Ar and H<sub>2</sub> were flowed for 20 min, galvanostatic electrolysis with 0.10–0.40 A cm<sup>-2</sup> was conducted using a IviumStat.XR apparatus (Ivium Technology) for 2 h at 298 K. Products of MCH, 1-methyl-1-cyclohexene (MCH-1-ene) and H<sub>2</sub>, were analyzed by gas chromatography techniques (GC-2025-FID (Shimadzu, HP-1 capillary column (0.25 mm i.d. × 100 m, Agilent Co.)) and GC-8A-TCD (Shimadzu, active carbon column (3 mm i.d. × 2.5 m))). The cathode potentials were monitored by the reference electrode of Ag/AgCl saturated KCl; however, all

electrode potentials in this paper are denoted against the SHE without  $iR$  correction. Electrocatalytic activities were evaluated by the FE(MCH) (Faradaic efficiency of MCH formation) and cathode potential during the electrolysis. The FE is defined as shown in eq 7.

$$FE = (\text{yield} \times F \times n/Q) \times 100\% \quad (7)$$

where  $F$  is the Faraday constant ( $96485 \text{ C mol}^{-1}$ ),  $n$  is the number of electrons, and  $Q$  is the charge passed.

**Characterization Studies.** Transmission electron microscope (TEM) measurement: TEM images were measured with a JEM-2010F electron microscope (JEOL, 200 kV) equipped with an EDX spectrometer (Genesis).

X-ray diffraction (XRD) measurement: XRD patterns were measured with a MiniFlex-600 X-ray diffraction instrument (Rigaku) with Cu  $K\alpha$  radiation (40 kV, 15 mA).

X-ray absorption fine structure (XAFS) measurement: XAFS spectra of Ru K edge and Ir  $L_{III}$  edge were measured in transmission mode at the beamlines NW10A of Photon Factory Advanced Ring (PF-AR) and BL9C of Photon Factory (PF) of the Institute for Materials Structures Science, High Energy Accelerator Research Organization (KEK-IMSS), Tsukuba, Japan, respectively. The X-ray beam was monochromated using a Si(311) and Si(111) double-crystal monochromator for Ru K edge and Ir  $L_{III}$  edge, respectively. The X-ray energy was calibrated using Ru metal ( $E_0 = 22119.3 \text{ eV}$ ) and Ir metal ( $E_0 = 11212 \text{ eV}$ ). XAFS samples were prepared by mixing the electrocatalyst and BN powders and pressing into a pellet (10 mm diameter). XAFS of the used MEA was measured in fluorescence mode. The MEA sample was fabricated by a method similar to that for the electrohydrogenation reaction except for the use of a 20 wt % Pd/KB/GDL anode instead of a 50 wt % Pt/KB/GDL anode because of overlap of the Pt  $L_{III}$  edge with the Ir  $L_{III}$  edge. Experimental procedures in detail are described as follows: after galvanostatic electrohydrogenation at  $0.2 \text{ A cm}^{-2}$  for 2 h, the MEA was removed from the electrolysis cell in an  $N_2$ -filled glovebox and enclosed in a plastic bag, which was used as a sample for XAFS measurement. The X-ray absorption near-edge structure (XANES) and extended X-ray absorption fine structure (EXAFS) spectra were analyzed using REX2000 software (Rigaku). The backscattering amplitudes and the phase shifts of Ru-Ru, Ru-Ir, Ru-O, Ir-Ir, Ir-Ru, and Ir-O were calculated using the FEFF program.<sup>15</sup> More details on the method of data reduction of EXAFS spectra are given in the [Supporting Information](#).

X-ray photoelectron spectroscopy (XPS) measurement: XPS spectra were measured using a JPS-9010MC instrument (JEOL) with Al  $K\alpha$  radiation (12 kV, 25 mA) and an analyzer pass energy of 30 eV. XPS spectra were calibrated by using the Au  $4f_{7/2}$  peak of mechanically mixed Au powder at 84.0 eV and normalized by the maximum intensity of respective spectra.

**Electrochemical Studies.** Cyclic voltammetry (CV) measurement: CVs of electrocatalysts were measured using a two-compartment cell divided by a glass filter. A working electrode was prepared by casting  $4.0 \mu\text{L}$  of electrocatalyst ink on a glassy-carbon electrode (i.d. 5.0 mm,  $0.19 \text{ mg}_{\text{catal}} \text{ cm}^{-2}$ ) and dried in air. The ink was prepared by ultrasonication of 2.0 mg of the electrocatalyst,  $20 \mu\text{L}$  of a 10 wt % Nafion dispersion and  $200 \mu\text{L}$  of acetone. The working electrode was set into 0.5 M  $\text{H}_2\text{SO}_4$  aqueous electrolyte in one compartment, and a counter electrode of Pt black/Pt wire and a reference electrode of Ag/AgCl saturated KCl were set into the same electrolyte in

another compartment. Before the CV measurements, electrochemical cleaning of the working electrode was applied between 0.0 and +0.8 V (SHE) at  $500 \text{ mV s}^{-1}$  for 100 cycles. We confirmed that hydrogen adsorption/oxidation currents did not decrease on the cleaning. Thereafter, CVs were measured between 0.0 and +0.8 V (SHE) at  $50 \text{ mV s}^{-1}$  for 3 cycles. The CV data were normalized by the geometric area of the GC electrode ( $0.20 \text{ cm}^2$ ). The CVs at the third cycle were reported.

Linear sweep voltammetry (LSV) measurement: Electrocatalytic activities for the hydrogen evolution reaction in 0.5 M aqueous  $\text{H}_2\text{SO}_4$  were evaluated by LSV in Ar. The working electrode was made by the same method as for the CV measurement. The counter electrode and reference electrode were the same as for the CV measurement. LSV measurements were carried out at  $1 \text{ mV s}^{-1}$  from +0.050 V (SHE) to negative potential for 3 cycles. The LSV data were normalized by the geometric area of the GC electrode ( $0.20 \text{ cm}^2$ ,  $j_{\text{geo}}$ ) and mass loading of Ir ( $j_{\text{Ir}}/\text{A mg}_{\text{Ir}}^{-1}$ ). The LSVs at the third cycle were reported.

**Evaluation of Heterogeneous Catalytic Activity for the Hydrogenation of TL.** The catalytic hydrogenation under pressure of  $\text{H}_2$  was conducted in an autoclave (volume 30 mL, i.d. 20 mm) with an inner tube of Pyrex glass (o.d. 20 mm, i.d. 17.6 mm, height 110 mm). A 10 mL portion of TL (contained 0.5 vol % *n*-heptane as internal standard), 1.0 mg of the catalyst, and a magnetic spin bar were placed in the inner tube. Air was purged by introduction of 0.7 MPa  $\text{N}_2$  and evacuation for several times. Thereafter,  $\text{H}_2$  was introduced to the autoclave under 6.0 MPa at 298 K and catalytic hydrogenation continued for 1 h. The reaction was stopped by evacuation of  $\text{H}_2$  at 1 h, and the reaction mixture was filtered. The filtrate was analyzed using a GC-2025-FID gas chromatograph. The products were MCH and MCH-1-ene, and other products were not detected. The consumption rate of  $\text{H}_2$  ( $-r(\text{H}_2)$ ) and the turnover frequency of Ru (TON(Ru)) calculated using the dispersion of metal particles ( $D$ ) obtained from TEM images were calculated as

$$-r(\text{H}_2) = 2r(\text{MCH-1-ene}) + 3r(\text{MCH}) \quad (8)$$

$$\text{TOF}(\text{Ru}) = -r(\text{H}_2) \times \text{aw}_{\text{Ru}} / (D_{\text{metal}} \times m_{\text{catal}} \times \text{wt}_{\text{Ru}}/100) \quad (9)$$

where  $r$  is the reaction rate of  $\text{H}_2$ ,  $\text{aw}_{\text{Ru}}$  is the atomic weight of Ru ( $101.07 \text{ g mol}^{-1}$ ),  $m_{\text{catal}}$  is the amount of catalyst (1.0 mg),  $\text{wt}_{\text{Ru}}$  is the mass loading of Ru in the catalyst, and  $D_{\text{metal}}$  is the metal dispersion obtained from TEM images; details are given in the [Supporting Information](#).

In addition, a similar TOF normalized by whole amount of Ru in catalyst (app-TOF(Ru)) was calculated as

$$\text{app-TOF}(\text{Ru}) = -r(\text{H}_2) \times \text{aw}_{\text{Ru}} / (m_{\text{catal}} \times \text{wt}_{\text{Ru}}/100) \quad (10)$$

## RESULTS AND DISCUSSION

**Electrohydrogenation of TL to MCH at Ru(x)-Ir(y)/KB Cathodes.** Figure 1 shows the electrocatalytic activities of the Ru(10)/KB, Ru(8)-Ir(2)/KB, Ru(5)-Ir(5)/KB, Ru(2)-Ir(8)/KB, and Ir(10)/KB cathodes for the electrohydrogenation of TL to MCH under galvanostatic electrolysis at  $0.20 \text{ A cm}^{-2}$  and 298 K. Figure 1a shows the time courses of the cathode potential during hydrogenation by the five cathodes. All

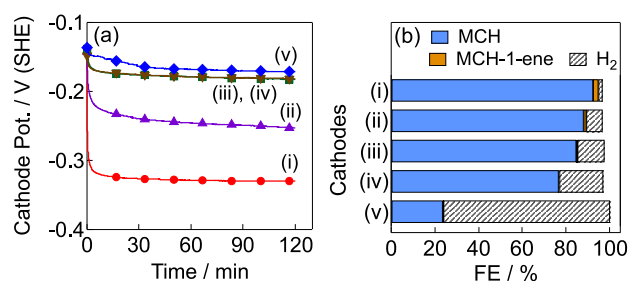
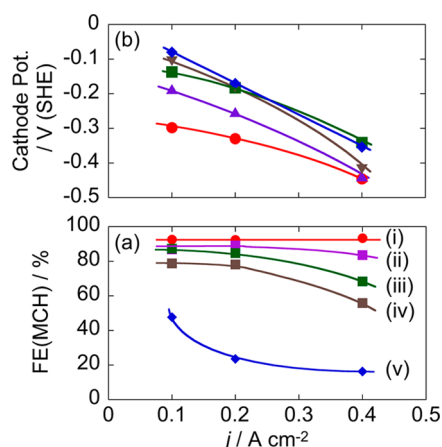


**Figure 1.** Electrohydrogenation of TL in galvanostatic electrolysis at  $0.2 \text{ A cm}^{-2}$  at  $\text{Ru}(x)\text{-Ir}(y)/\text{KB}$  cathodes: (a) time profile of cathode potential during electrolysis; (b) Faradaic efficiency of MCH, MCH-1-ene, and  $\text{H}_2$  formation. Legend to cathodes: (i)  $\text{Ru}(10)/\text{KB}$ ; (ii)  $\text{Ru}(8)\text{-Ir}(2)/\text{KB}$ ; (iii)  $\text{Ru}(5)\text{-Ir}(5)/\text{KB}$ ; (iv)  $\text{Ru}(2)\text{-Ir}(8)/\text{KB}$ ; (v)  $\text{Ir}(10)/\text{KB}$ .

cathode potentials were very stable after 10 min. The order of cathode potential was  $\text{Ru}(10)/\text{KB} < \text{Ru}(8)\text{-Ir}(2)/\text{KB} < \text{Ru}(5)\text{-Ir}(5)/\text{KB} < \text{Ru}(2)\text{-Ir}(8)/\text{KB} < \text{Ir}(10)/\text{KB} < +0.16 \text{ V}$  (standard potential) at  $0.20 \text{ A cm}^{-2}$  electrolysis. Figure 1b shows FEs of the products MCH, MCH-1-ene, and  $\text{H}_2$ . The sum of  $\text{FE}(\text{MCH})$ ,  $\text{FE}(\text{MCH-1-ene})$ , and  $\text{FE}(\text{H}_2)$  was 100% for all cathodes. At the  $\text{Ru}(10)/\text{KB}$  cathode, a very high  $\text{FE}(\text{MCH})$  of 94%, the same as the selectivity to MCH, was observed; however, the working potential of the  $\text{Ru}(10)/\text{KB}$  cathode at  $-0.330 \text{ V}$  was far to the negative side from the standard potential of  $+0.16 \text{ V}$  (eq 4). A large overpotential of  $0.49 \text{ V}$  at the  $\text{Ru}(10)/\text{KB}$  cathode is a disadvantage. In contrast to the  $\text{Ru}(10)/\text{KB}$  cathode, the hydrogen evolution reaction dominantly proceeded at the  $\text{Ir}(10)/\text{KB}$  cathode, though the working potential was relatively positive ( $-0.171 \text{ V}$ ). When 2 wt % of Ir was loaded with a 8 wt % of Ru on KB ( $\text{Ru}(8)\text{-Ir}(2)/\text{KB}$  cathode), the working potential shifted to positive potential at  $-0.253 \text{ V}$  while a high  $\text{FE}(\text{MCH})$  of 90% was retained. A synergy of Ru and Ir was observed on the working potential and  $\text{FE}(\text{MCH})$ . Therefore, the ratios of Ru and Ir were changed to 5:5 and 2:8; on the  $\text{Ru}(5)\text{-Ir}(5)/\text{KB}$  cathode, the working potential shifted to being more positive at  $-0.183 \text{ V}$  with 86% for  $\text{FE}(\text{MCH})$ , and on the  $\text{Ru}(2)\text{-Ir}(8)/\text{KB}$  cathode, the  $\text{FE}(\text{MCH})$  slightly decreased to 78% at  $-0.182 \text{ V}$ , similar to that for the  $\text{Ru}(5)\text{-Ir}(5)/\text{KB}$  cathode. As described above, we found that the working potential shifted positively without a significant decrease in  $\text{FE}(\text{MCH})$  by mixing Ir and Ru on KB.

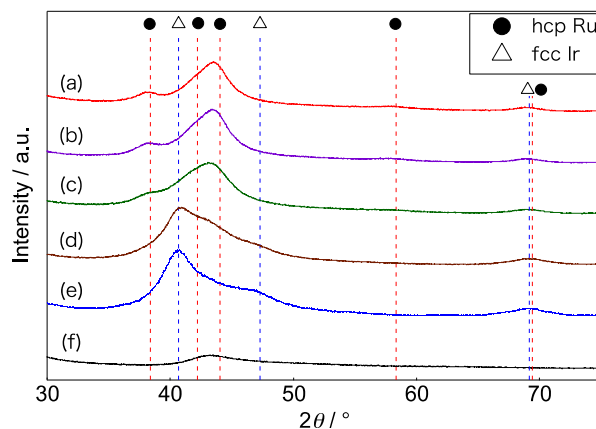
In order to confirm the above synergy of Ru and Ir, the influence of the Pt/KB anode on the cathode reaction was studied. A 20 wt % Pd/KB anode instead of the Pt/KB anode was applied for electrohydrogenation, and the same results were obtained. This indicated no influence of the Pt/KB anode on the synergy of Ru and Ir. The synergy of Ru and Ir on the electrohydrogenation is attractive; therefore, studies have been done to reveal the mechanism of the synergy and electrocatalysis.

Figure 2 shows the effects of current densities ( $j$ ) on the galvanostatic electrohydrogenation at the  $\text{Ru}(x)\text{-Ir}(y)/\text{KB}$  cathodes at 298 K. FEs of MCH-1-ene and  $\text{H}_2$  are indicated in Figure S1 in the Supporting Information. At the  $\text{Ru}(10)/\text{KB}$  cathode,  $\text{FE}(\text{MCH})$  values were always high without dependence on  $j$  values. A high  $\text{FE}(\text{MCH})$  of 93% was observed at  $0.40 \text{ A cm}^{-2}$ . In contrast, the  $\text{FE}(\text{MCH})$  value was only 48% even at  $0.10 \text{ A cm}^{-2}$  at the  $\text{Ir}(10)/\text{KB}$  cathode, and it decreased with an increase in  $j$ . At the  $\text{Ru}(8)\text{-Ir}(2)/\text{KB}$ ,  $\text{Ru}(5)\text{-Ir}(5)/\text{KB}$ , and  $\text{Ru}(2)\text{-Ir}(8)/\text{KB}$  cathodes,  $\text{FE}(\text{MCH})$  values were almost constant between  $0.10$  and  $0.20 \text{ A cm}^{-2}$  and slightly decreased at  $0.40 \text{ A cm}^{-2}$ . The order of  $\text{FE}(\text{MCH})$  values was  $\text{Ru}(10)/\text{KB} > \text{Ru}(8)\text{-Ir}(2)/\text{KB} > \text{Ru}(5)\text{-Ir}(5)/\text{KB} > \text{Ru}(2)\text{-Ir}(8)/\text{KB} > \text{Ir}(10)/\text{KB}$  without dependence on  $j$  value. The cathodes containing more Ru show higher  $\text{FE}(\text{MCH})$  values. For working cathode potentials, the order of the cathodes was reverse at  $0.10$  and  $0.20 \text{ A cm}^{-2}$ . The cathodes containing more Ir show more positive working potentials. The cathode potentials at  $0.40 \text{ A cm}^{-2}$  were extremely negative for all cathodes and should contain different overvoltages of activation, resistance, and concentration, which may be the reason a simple rule cannot be applied to relations between  $\text{Ru}/(\text{Ru} + \text{Ir})$  and working potentials.



**Figure 2.** Effects of electrolysis current densities ( $j$ ) on (a)  $\text{FE}(\text{MCH})$  and (b) cathode potential during the electrohydrogenation of TL at  $\text{Ru}(x)\text{-Ir}(y)/\text{KB}$  cathodes. Legend to cathodes: (i)  $\text{Ru}(10)/\text{KB}$ ; (ii)  $\text{Ru}(8)\text{-Ir}(2)/\text{KB}$ ; (iii)  $\text{Ru}(5)\text{-Ir}(5)/\text{KB}$ ; (iv)  $\text{Ru}(2)\text{-Ir}(8)/\text{KB}$ ; (v)  $\text{Ir}(10)/\text{KB}$ .

**Characterization of  $\text{Ru}(x)\text{-Ir}(y)/\text{KB}$  Electrocatalyst.** Figure 3 shows XRD patterns of the  $\text{Ru}(x)\text{-Ir}(y)/\text{KB}$  electrocatalysts. In the XRD patterns of the  $\text{Ru}(10)/\text{KB}$  and  $\text{Ir}(10)/\text{KB}$  electrocatalysts, we observed diffraction patterns assigned to hcp Ru and fcc Ir, respectively. Crystallite diameters of Ru and Ir were estimated as 3–4 nm from  $\text{Ru}(100)$ ,  $\text{Ru}(102)$ , and  $\text{Ru}(110)$  and 2.5–3 nm from  $\text{Ir}(111)$  and  $\text{Ir}(220)$ , respectively. The XRD patterns of the  $\text{Ru}(8)\text{-Ir}(2)/\text{KB}$ ,  $\text{Ru}(5)\text{-Ir}(5)/\text{KB}$ , and  $\text{Ru}(2)\text{-Ir}(8)/\text{KB}$  cathodes,  $\text{FE}(\text{MCH})$  values were almost constant between  $0.10$  and  $0.20 \text{ A cm}^{-2}$  and slightly decreased at  $0.40 \text{ A cm}^{-2}$ . The order of  $\text{FE}(\text{MCH})$  values was  $\text{Ru}(10)/\text{KB} > \text{Ru}(8)\text{-Ir}(2)/\text{KB} > \text{Ru}(5)\text{-Ir}(5)/\text{KB} > \text{Ru}(2)\text{-Ir}(8)/\text{KB} > \text{Ir}(10)/\text{KB}$  without dependence on  $j$  value. The cathodes containing more Ru show higher  $\text{FE}(\text{MCH})$  values. For working cathode potentials, the order of the cathodes was reverse at  $0.10$  and  $0.20 \text{ A cm}^{-2}$ . The cathodes containing more Ir show more positive working potentials. The cathode potentials at  $0.40 \text{ A cm}^{-2}$  were extremely negative for all cathodes and should contain different overvoltages of activation, resistance, and concentration, which may be the reason a simple rule cannot be applied to relations between  $\text{Ru}/(\text{Ru} + \text{Ir})$  and working potentials.



**Figure 3.** XRD patterns of (a)  $\text{Ru}(10)/\text{KB}$ , (b)  $\text{Ru}(8)\text{-Ir}(2)/\text{KB}$ , (c)  $\text{Ru}(5)\text{-Ir}(5)/\text{KB}$ , (d)  $\text{Ru}(2)\text{-Ir}(8)/\text{KB}$ , and (e)  $\text{Ir}(10)/\text{KB}$  electrocatalysts and (f) KB material.

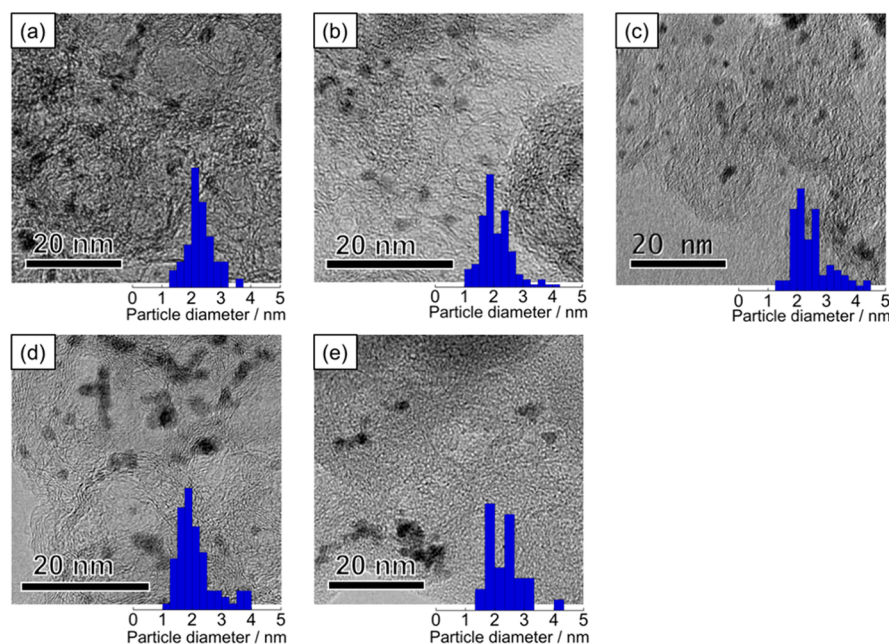


**Figure 4.** TEM images and distribution of particle diameters of (a) Ru(10)/KB, (b) Ru(8)-Ir(2)/KB, (c) Ru(5)-Ir(5)/KB, (d) Ru(2)-Ir(8)/KB, and (e) Ir(10)/KB electrocatalysts.

Ir(2)/KB and Ru(5)-Ir(5)/KB electrocatalysts were similar to that of Ru(10)/KB electrocatalyst. However, the diffraction peaks slightly shifted to a lower angle to compare with Ru(10)/KB electrocatalyst (see Figure S2 in the Supporting Information), which suggested expansion of lattice parameters of hcp structure and formation of a hcp-structured solid-solution alloy of Ru and Ir.<sup>16</sup> The XRD pattern of the Ru(2)-Ir(8)/KB electrocatalyst showed diffraction patterns assigned to fcc and hcp structures. This suggested that there were Ru-Ir alloy and monometallic Ir (fcc) on the Ru(2)-Ir(8)/KB electrocatalyst. The formation of Ru-Ir alloy was also proposed by the results of TEM-EDS and EXAFS analysis, as discussed later.

Figure 4 shows TEM images of Ru(*x*)-Ir(*y*)/KB electrocatalysts and distributions of particle diameters. For all samples, distributions of nanoparticle diameter were relatively wide: 1.5–4 nm. The average particle diameters of Ru(10)/KB, Ru(8)-Ir(2)/KB, Ru(5)-Ir(5)/KB, Ru(2)-Ir(8)/KB, and Ir(10)/KB electrocatalysts were 2.3, 2.1, 2.5, 2.1, and 2.3 nm, respectively, and were very similar values. The mass ratios of Ru and Ir on the Ru(8)-Ir(2)/KB, Ru(5)-Ir(5)/KB and Ru(2)-Ir(8)/KB samples were determined using EDS analysis (Figure S3, Supporting Information). The mass ratio of Ru:Ir at particles on the Ru(8)-Ir(2)/KB was 70:30 to 80:20. That on the Ru(5)-Ir(5)/KB was 50:50. These ratios were very similar to the ratios in the preparation conditions, indicating that Ru and Ir formed a uniform Ru-Ir alloy on the Ru(8)-Ir(2)/KB and Ru(5)-Ir(5)/KB electrocatalysts. In the Ru(2)-Ir(8)/KB sample, the mass ratios at particles were from 35:65 to 0:100. This wide distributions of the mass ratio of Ru and Ir indicates that nanoparticles of Ru-Ir alloy and monometallic Ir are on the Ru(2)-Ir(8)/KB sample.

Parts a and b of Figure 5 and Figure S5 show Ru K-edge XANES spectra, Fourier transform of EXAFS spectra, and EXAFS oscillations, respectively. Parts a and b of Figure 6 and Figure S6 show Ir L<sub>III</sub>-edge XANES spectra, Fourier transform of EXAFS spectra, and EXAFS oscillations, respectively. In addition to Ru(*x*)-Ir(*y*)/KB electrocatalysts, Ru metal, RuO<sub>2</sub>,

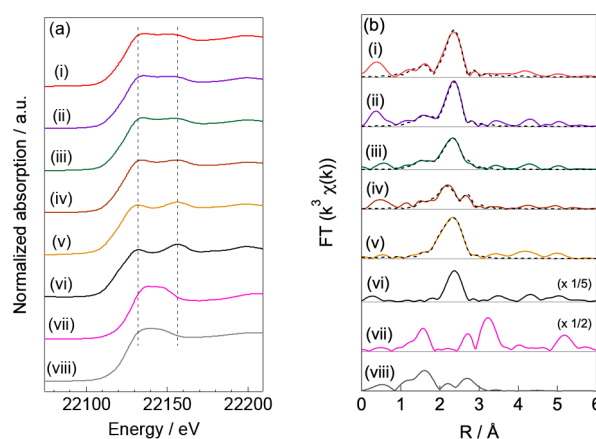


**Figure 5.** Ru K-edge (a) XANES spectra and (b) Fourier transform of  $k^3$ -weighted EXAFS spectra (solid line, observed spectra; dashed line, fitting) of (i) Ru(10)/KB, (ii) Ru(8)-Ir(2)/KB, (iii) Ru(5)-Ir(5)/KB, and (iv) Ru(2)-Ir(8)/KB electrocatalysts, (v) Ru(5)-Ir(5)/KB-used, and (vi) Ru metal, (vii) RuO<sub>2</sub>, and (viii) RuO<sub>2</sub>·*n*H<sub>2</sub>O reference materials.

RuO<sub>2</sub>·*n*H<sub>2</sub>O, Ir metal, and IrO<sub>2</sub> were measured as reference materials. As shown in Figure 5a(i),a(vi), the shape of the XANES spectrum of the Ru(10)/KB electrocatalyst was similar to that of Ru metal. The XANES spectra of the Ru(8)-Ir(2)/KB, Ru(5)-Ir(5)/KB, and Ru(2)-Ir(8)/KB electrocatalysts were also similar to that of Ru metal. However, the intensities around 22133 eV of the electrocatalysts were stronger than that of Ru metal, which indicated partial oxidation of Ru for the electrocatalysts. No major differences in Ru K-edge XANES spectra were observed among Ru(10)/KB, Ru(8)-Ir(2)/KB, Ru(5)-Ir(5)/KB, and Ru(2)-Ir(8)/KB electrocatalysts regardless of Ru/(Ru+Ir). In the case of Ir (Figure 6a), the white-line intensities of the electrocatalysts were stronger than that of Ir metal and weaker than that of IrO<sub>2</sub>, which indicated partial oxidation of Ir for the electrocatalysts. There were no major differences in the Ir L<sub>III</sub>-edge XANES

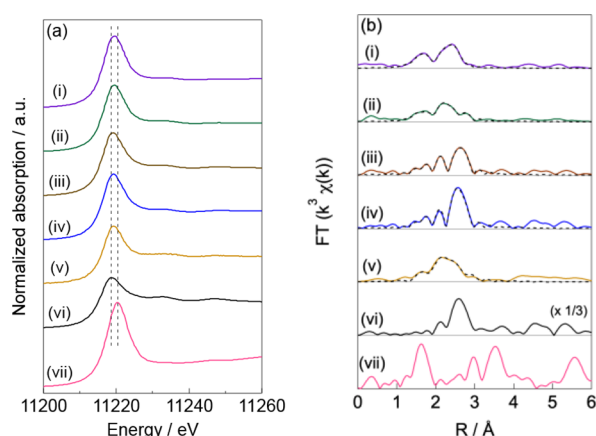


**Figure 6.** Ir  $L_{III}$ -edge (a) XANES spectra and (b) Fourier transform of  $k^3$ -weighted EXAFS spectra (solid line, observed spectra; dashed line, fitting) of (i) Ru(8)-Ir(2)/KB, (ii) Ru(5)-Ir(5)/KB, (iii) Ru(2)-Ir(8)/KB, and (iv) Ir(10)/KB electrocatalysts, (v) Ru(5)-Ir(5)/KB-used, and (vi) Ir metal and (vii) IrO<sub>2</sub> reference materials.

spectra of all electrocatalysts. In the case of Ru K-edge EXAFS spectra (Figure 5b), a peak at 2.4 Å observed for Ru metal (vi) was assigned to the first neighboring atom of Ru. Peaks at 1.6 Å observed for RuO<sub>2</sub> (vii) and RuO<sub>2</sub>·*n*H<sub>2</sub>O (viii) were assigned to the first neighboring atom of O. In the spectrum of Ru(10)/KB electrocatalyst, peaks at 2.4 and 1.6 Å were observed, which indicated a mixture of Ru metal and oxidized Ru species on the Ru(10)/KB electrocatalyst. Peaks at 1.6 and 2.1–2.4 Å were observed in the spectra of Ru(8)-Ir(2)/KB, Ru(5)-Ir(5)/KB, and Ru(2)-Ir(8)/KB electrocatalysts, and the shape of spectra at 2–3 Å changed depending on Ru/(Ru+Ir), which indicated a change in the coordination environment around Ru. Results of a curve fitting analysis of the EXAFS spectra are given in Table 1. More detailed fitting results (edge shifts and Debye–Waller factors) are shown in Tables S1 and S2 in the Supporting Information. The coordination number of Ru around Ru (CN(Ru–Ru)) decreased and the CN(Ru–Ir) increased as Ru/(Ru+Ir) decreased. CN(Ru–O) values were almost constant. In the case of Ir (Figure 6b), a peak at 2.6 Å observed at Ir metal was assigned to the first neighboring atom of Ir, and a peak at 1.6 Å observed at IrO<sub>2</sub> was assigned to the first neighboring atom of O. In the spectrum of Ir(10)/KB electrocatalyst, peaks at 2.6 and 1.6 Å were observed, which indicated a mixture of Ir metal and oxidized Ir species on the Ir(10)/KB electrocatalyst. Peaks at 1.6 and 2–3 Å were observed in the spectra of Ru(8)-Ir(2)/KB, Ru(5)-Ir(5)/KB, and Ru(2)-Ir(8)/KB electrocatalysts. As Ru/(Ru+Ir) increased, the CN(Ir–Ir) value decreased and the CN(Ir–Ru) value increased as shown in Table 1. These EXAFS analyses

clearly indicated that Ru and Ir formed an alloy structure in the Ru(8)-Ir(2)/KB, Ru(5)-Ir(5)/KB, and Ru(2)-Ir(8)/KB electrocatalysts and that the Ru/Ir composition of Ru–Ir alloy changed according to Ru/Ir ratios under the preparation conditions.

XPS spectra were measured to obtain knowledge about the electronic states of Ru and Ir in detail. Bulk compositions of Ru and Ir corresponded to those obtained from XPS data (Figure S4). Parts a and b of Figure 7 show XPS spectra of the

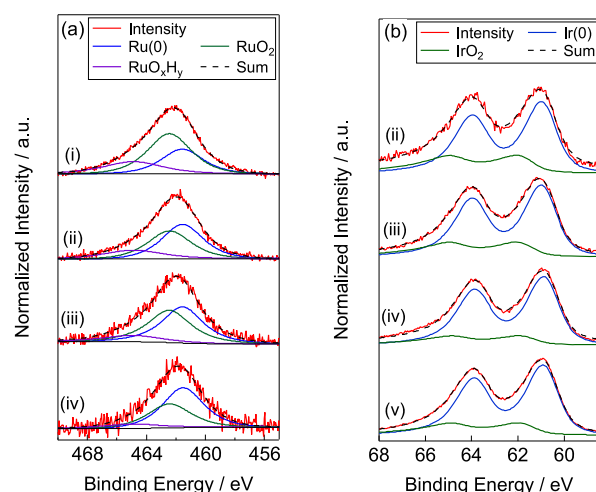


**Figure 7.** XPS spectra of (a) Ru 3p<sub>3/2</sub> and (b) Ir 4f regions: (i) Ru(10)/KB, (ii) Ru(8)-Ir(2)/KB, (iii) Ru(5)-Ir(5)/KB, (iv) Ru(2)-Ir(8)/KB, and (v) Ir(10)/KB electrocatalysts.

Ru 3p<sub>3/2</sub> and Ir 4f regions of the Ru(*x*)-Ir(*y*)/KB electrocatalysts, respectively. For all electrocatalysts, metallic Ru and oxidized Ru species were detected. The XPS spectra were deconvoluted to three Gaussian–Lorentzian functions, which are assigned to Ru(0) (461.6 eV), RuO<sub>2</sub> (462.4 eV), and hydrous Ru oxide species (RuO<sub>*x*</sub>H<sub>*y*</sub>).<sup>17,18</sup> Though ratios of metallic Ru slightly increased with a decrease in Ru content of Ru–Ir/KB electrocatalysts, the binding energy of electrons in Ru was constant. Major differences in electronic states of Ru were not observed for various Ru–Ir/KB electrocatalysts. In the case of the Ir 4f region, metallic Ir and oxidized Ir species were observed. The spectra of the Ir 4f region were analyzed using a linear combination fitting (LCF) of reference spectra of Ir metal and IrO<sub>2</sub> because they are difficult to deconvolute using theoretical functions due to complex satellite peaks of the Ir 4f region.<sup>19</sup> The binding energy of electrons in Ir was constant. No major differences in XPS spectra were observed for all Ru–Ir/KB electrocatalysts. XPS results indicated that there were no strong electronic interactions between Ru and Ir in the Ru–Ir

**Table 1.** Curve-Fitting Analysis of Ru K-Edge and Ir  $L_{III}$ -Edge EXAFS Spectra of Ru(*x*)-Ir(*y*)/KB Electro-catalysts

|                     | Ru K edge |     |      |     |      |     | Ir $L_{III}$ edge |     |      |     |      |     |
|---------------------|-----------|-----|------|-----|------|-----|-------------------|-----|------|-----|------|-----|
|                     | Ru        |     | Ir   |     | O    |     | Ru                |     | Ir   |     | O    |     |
|                     | R/Å       | CN  | R/Å  | CN  | R/Å  | CN  | R/Å               | CN  | R/Å  | CN  | R/Å  | CN  |
| Ru(10)/KB           | 2.67      | 5.5 |      |     | 1.97 | 1.4 |                   |     |      |     |      |     |
| Ru(8)-Ir(2)/KB      | 2.67      | 4.2 | 2.65 | 0.6 | 2.03 | 1.7 | 2.66              | 2.4 | 2.64 | 1.3 | 2.00 | 2.9 |
| Ru(5)-Ir(5)/KB      | 2.67      | 3.7 | 2.66 | 2.3 | 1.97 | 1.0 | 2.66              | 2.3 | 2.66 | 3.1 | 2.00 | 2.0 |
| Ru(2)-Ir(8)/KB      | 2.67      | 3.4 | 2.67 | 5.2 | 1.94 | 0.3 | 2.67              | 1.3 | 2.70 | 5.3 | 2.00 | 1.5 |
| Ir(10)/KB           |           |     |      |     |      |     |                   |     | 2.69 | 7.1 | 2.00 | 1.3 |
| Ru(5)-Ir(5)/KB-used | 2.66      | 3.6 | 2.66 | 2.4 |      |     | 2.66              | 3.3 | 2.65 | 4.5 | 2.03 | 1.1 |

alloy. This weak interaction between Ru and Ir may be due to the similar electronegativities of Ru and Ir.<sup>20</sup>

The XPS and XAFS results revealed the contents of oxidized Ru and oxidized Ir species in all electrocatalysts. These oxidized species should form by exposure in air after the catalyst preparations. Therefore, the observed oxidation states of Ru and Ir differ from the real character of the catalyst during the electrohydrogenation at negative potentials. The electrohydrogenation reactions are conducted at potentials lower than the standard redox potentials of Ru/RuO<sub>2</sub> and Ir/IrO<sub>2</sub>,<sup>21</sup> which indicates the reduction states of the catalyst. To confirm the oxidation states of Ru and Ir during the electrohydrogenation of TL, XAFS measurements of used Ru(5)-Ir(5)/KB/GDL|Nafion117|Pd/KB/GDL (Ru(5)-Ir(5)/KB-used) was conducted without exposure to air.

Figure 5a(v),b(v) and Figure S5(v) show Ru K-edge XANES spectra, Fourier transform of EXAFS spectra, and EXAFS oscillations, respectively. Figure 6a(v),b(v) and Figure S6(v) show Ir L<sub>III</sub>-edge XANES spectra, Fourier transform of EXAFS spectra, and EXAFS oscillations, respectively. The shape of Ru K-edge XANES spectra of the Ru(5)-Ir(5)/KB-used (Figure 5a(v)) was very similar to that of Ru metal, which indicated electrochemical reduction of oxidized Ru species to metallic Ru. In the case of Ir L<sub>III</sub>-edge XANES spectra (Figure 6a), the white-line intensity of the Ru(5)-Ir(5)/KB-used was smaller than that of Ru(5)-Ir(5)/KB electrocatalysts though it was slightly stronger than that of Ir metal, which indicated electrochemical reduction of oxidized Ir species. The shape of Ru K-edge and Ir L<sub>III</sub>-edge EXAFS spectra of the Ru(5)-Ir(5)/KB-used differed from that of the Ru(5)-Ir(5)/KB electrocatalysts. In the curve-fitting analysis of the EXAFS spectra of Ru(5)-Ir(5)/KB-used (Table 1), coordination of Ru and Ir around Ru and coordination of Ru and Ir around Ir were observed, which indicated that Ru and Ir kept the Ru-Ir alloy after the electrohydrogenation. Furthermore, no coordination of oxygen around Ru was observed at the EXAFS spectrum of the Ru(5)-Ir(5)/KB-used. Though the CN(Ir-O) value of the Ru(5)-Ir(5)/KB-used was not zero, it was smaller than that of Ru(5)-Ir(5)/KB electrocatalyst. These EXAFS results correspond to results of XANES spectra. A small amount of oxidized Ir species may remain after the electrohydrogenation or may reoxidize with water after the electrohydrogenation. Though the origin of oxidized Ir species was not clear, these XAFS results indicated that the majority of Ru and Ir was in a metallic state during the electrohydrogenation.

**Electrochemical Studies of Ru(x)-Ir(y)/KB Electrocatalysts.** To obtain knowledge of the surface structure of Ru(x)-Ir(y)/KB electrocatalysts, CVs of hydrogen adsorption/desorption feature were obtained. Figure 8 shows CVs of the Ru(x)-Ir(y)/KB electrocatalysts coated on glassy-carbon electrodes in 0.5 M H<sub>2</sub>SO<sub>4</sub> aqueous solution. At the Ru(10)/KB electrocatalyst (Figure 8a), a weak oxidation/reduction couple of Ru was observed between 0.2 and 0.6 V (SHE).<sup>22</sup> At the Ir(10)/KB electrocatalyst (Figure 8e), redox couples assigned to electrochemical adsorption/desorption of hydrogen species were observed between 0.0–0.3 V (SHE). At the Ru(8)-Ir(2)/KB (b), Ru(5)-Ir(5)/KB (c) and Ru(2)-Ir(8)/KB (d) electrocatalysts, redox couples of Ru and hydrogen were overserved. Because no redox couple of hydrogen was observed at the Ru(10)/KB electrocatalyst, the redox couples of hydrogen on the Ru(8)-Ir(2)/KB, Ru(5)-Ir(5)/KB, and Ru(2)-Ir(8)/KB electrocatalysts should be due to electrocatalysis of the Ir surface. Therefore, a coulomb for

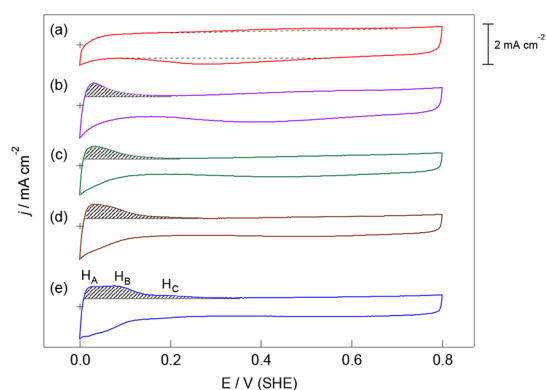


**Figure 8.** CVs (50 mV s<sup>-1</sup>) of (a) Ru(10)/KB, (b) Ru(8)-Ir(2)/KB, (c) Ru(5)-Ir(5)/KB, (d) Ru(2)-Ir(8)/KB, and (e) Ir(10)/KB electrocatalysts coated on a glassy-carbon electrode in 0.5 M H<sub>2</sub>SO<sub>4</sub>. Origins of respective CVs are denoted with “+”.

the hydrogen desorption ( $Q_H$ , shaded area in Figure 8) is proportional to the electrochemical active surface area (ECSA) of Ir. The  $Q_H$  values of Figure 8 were plotted as a function of Ru/(Ru+Ir) in Figure 9. The  $Q_H$  increased with a decrease in

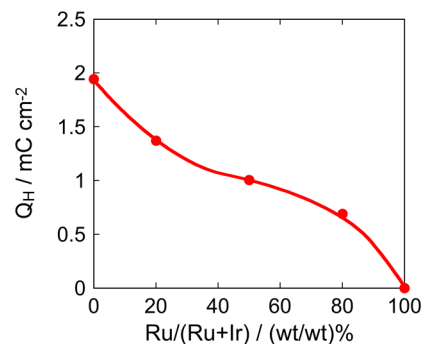


**Figure 9.** Charge passed for hydrogen desorption ( $Q_H$ ) observed in CVs in 0.5 M H<sub>2</sub>SO<sub>4</sub>.

Ru/(Ru+Ir). In other words, the ECSA of Ir increased with a decrease in Ru/(Ru+Ir). The  $Q_H$  curve was a weak sigmoid but was almost straight. This indicated that the Ru/Ir composition at the surface of the Ru-Ir alloy is similar to that of the bulk of the Ru-Ir alloy. In addition, three peaks of H<sub>ad</sub> were observed from the shape of CV of Ir(10)/KB (Figure 8e). They are denoted as H<sub>A</sub>, H<sub>B</sub>, and H<sub>C</sub> from negative potentials. At the Ru(8)-Ir(2)/KB, Ru(5)-Ir(5)/KB, and Ru(2)-Ir(8)/KB electrocatalysts, current peaks of H<sub>A</sub> in CVs Figure 8b–d seemed to be constant and independent of Ru/(Ru+Ir). In contrast, current peaks of H<sub>B</sub> and H<sub>C</sub> decreased with and increase in Ru/(Ru+Ir). From previous reports, we assigned H<sub>A</sub> as H<sub>ad</sub> adsorbed at an on-top site of Ir and H<sub>B</sub> and H<sub>C</sub> as H<sub>ad</sub> adsorbed at bridge and hollow sites of Ir, respectively.<sup>23,24</sup> On a large Ir ensemble of the Ir(10)/KB, the three hydrogen species H<sub>A</sub>, H<sub>B</sub>, and H<sub>C</sub> were observed in the CV of Figure 8e. In a mixture of Ir and Ru, H<sub>B</sub> and H<sub>C</sub> decreased because the Ir ensemble decreased and bridge and hollow sites decreased. When the Ir ensemble significantly decreased, Ir species were isolated but H<sub>A</sub> species at the on-top site of Ir remained. The above observations indicated that Ir and Ru were well mixed in all components.

The hydrogen evolution reaction was evaluated by LSV in 0.5 M H<sub>2</sub>SO<sub>4</sub>, as shown in Figure 10. Figure 10a shows LSVs

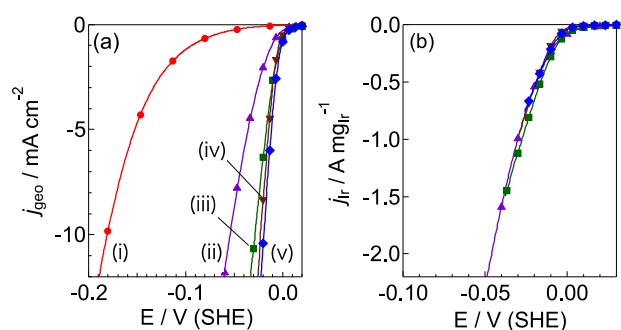


**Figure 10.** LSVs of Ru(*x*)-Ir(*y*)/KB electrocatalysts at 0.5 M H<sub>2</sub>SO<sub>4</sub>. Currents are normalized by (a) geometric area and (b) mass loading of Ir. Legend for electrocatalysts: (i) Ru(10)/KB; (ii) Ru(8)-Ir(2)/KB; (iii) Ru(5)-Ir(5)/KB; (iv) Ru(2)-Ir(8)/KB; (v) Ir(10)/KB.

normalized by the geometric area of electrode ( $j_{\text{geo}}$ ). Ru(10)/KB showed a large overpotential for the hydrogen evolution reaction. As Ru/(Ru+Ir) decreased, the overpotentials for the hydrogen evolution drastically decreased. The Ru(5)-Ir(5)/KB and Ru(2)-Ir(8)/KB electrocatalysts were as active as the Ir(10)/KB electrocatalyst. Figure 10b shows LSVs of Ru(8)-Ir(2)/KB, Ru(5)-Ir(5)/KB, Ru(2)-Ir(8)/KB, and Ir(10)/KB electrocatalysts normalized by the mass loading of Ir ( $j_{\text{Ir}}$ ). The  $j_{\text{Ir}}$  values of the Ru(8)-Ir(2)/KB, Ru(5)-Ir(5)/KB, Ru(2)-Ir(8)/KB, and Ir(10)/KB electrocatalysts were almost the same, which indicated that hydrogen evolution reaction proceeded on the Ir site of the Ru-Ir alloy. Furthermore, the similar  $j_{\text{Ir}}$  values of Ru(8)-Ir(2)/KB, Ru(5)-Ir(5)/KB, Ru(2)-Ir(8)/KB, and Ir(10)/KB suggest that the specific activity of Ir for hydrogen evolution is very similar to those of the Ir particle and Ru-Ir alloy particle. In other words, the nature of Ir at the surface of the Ir particle and that at the surface of the Ru-Ir alloy particle were very similar.

**Catalytic Hydrogenation Activity of Ru(*x*)-Ir(*y*)/KB Catalysts and Reaction Mechanisms of the Electrohydrogenation of TL to MCH.** In our previous work,<sup>13</sup> we proposed a primitive reaction mechanism for the electrohydrogenation of TL to MCH as follows: (i) formation of H<sub>ad</sub> on the metal surface by the electrochemical reduction of H<sup>+</sup> (H<sup>+</sup> + e<sup>-</sup> + \* → H<sub>ad</sub>), (ii) TL was adsorbed on the catalyst surface (TL + \* → TL<sub>ad</sub>), and (iii) TL<sub>ad</sub> and H<sub>ad</sub> catalytically reacted to form MCH (TL<sub>ad</sub> + 6H<sub>ad</sub> → MCH + \*). H<sub>2</sub> formation proceeds via (iv) a coupling of H<sub>ad</sub> (2H<sub>ad</sub> → H<sub>2</sub> + \*). On the basis of the mechanism, we considered that the overpotential for the electrohydrogenation is determined by the overpotential for H<sub>ad</sub> formation (i). It is well-known that the hydrogen evolution reaction also proceeds via the electrochemical formation of H<sub>ad</sub>.<sup>25–27</sup> Therefore, electrocatalytic activities for the hydrogen evolution reaction should be closely related to the electrohydrogenation activity. As mentioned above, Ru(10)/KB showed a large overpotential for the electrochemical hydrogen evolution, which indicated a large overpotential for formation of H<sub>ad</sub> on Ru. This is the reason Ru(10)/KB showed a large overpotential for the electrohydrogenation of TL. The Ru(5)-Ir(5)/KB and Ru(2)-Ir(8)/KB electrocatalysts showed as small an overpotential as the Ir(10)/KB electrocatalyst, which is the reason Ru(5)-Ir(5)/KB and Ru(2)-Ir(8)/KB cathodes showed smaller overpotentials for the electrohydrogenation of TL similar to the overpotential for H<sub>2</sub> evolution at the Ir(10)/KB cathode.

On the basis of the above mechanism, FE(MCH) should be determined by the ratio of the chemical reaction rates of the hydrogenation at the surface (iii) and the coupling of H<sub>ad</sub> (iv). It is known that the catalytic hydrogenation of aromatics under pressure of H<sub>2</sub> proceeds via a catalytic surface reaction with dissociative adsorption species of H<sub>2</sub> and adsorbed aromatics.<sup>28–30</sup> Therefore, the catalytic hydrogenation activity is closely related to the electrohydrogenation activity. To obtain information about the synergy of Ru and Ir in the electrohydrogenation of TL to MCH, catalytic hydrogenation activities of Ru(*x*)-Ir(*y*)/KB catalysts were evaluated at 298 K under 6.0 MPa of H<sub>2</sub> (Table 2). Under high-pressure

**Table 2.** Catalytic Activities of Ru(*x*)-Ir(*y*)/KB Catalysts for the Catalytic Hydrogenation of TL in Liquid Phase under 6.0 MPa of H<sub>2</sub><sup>a</sup>

| catalyst       | yield/mmol |           | -r(H <sub>2</sub> )/mmol h <sup>-1</sup> <sup>b</sup> | TOF(Ru)/10 <sup>4</sup> h <sup>-1</sup> |
|----------------|------------|-----------|---|---|
|                | MCH        | MCH-1-ene |   |   |
| Ru(10)/KB      | 6.8        | 1.0       | 23  | 4.5                                     |
| Ru(8)-Ir(2)/KB | 4.6        | 0.6       | 15  | 3.2                                     |
| Ru(5)-Ir(5)/KB | 3.4        | 0.32      | 11  | 4.6                                     |
| Ru(2)-Ir(8)/KB | 1.0        | 0.1       | 3.1   | 2.9                                     |
| Ir(10)/KB      | 0.014      | trace     | 0.042   |   |

<sup>a</sup>Conditions: catalyst, 1.0 mg; reactant, toluene 10 mL (contains 0.5 vol % *n*-heptane as internal standard); T = 298 K; p(H<sub>2</sub>) = 6.0 MPa; reaction time 1 h. <sup>b</sup>consumption rate of H<sub>2</sub>

conditions, the catalytic hydrogenation activity is determined by the rate of the surface reaction between H<sub>ad</sub> and TL<sub>ad</sub>. Ru(10)/KB showed the highest catalytic activity for the catalytic hydrogenation of TL. As shown in Figure S7 of the Supporting Information, a short induction period of about 10 min was observed and the yield of MCH linearly increased until 4 h. This catalytic hydrogenation indicated a fast surface reaction between H<sub>ad</sub> and TL<sub>ad</sub> on the Ru surface. Adsorption energies of H<sub>ad</sub> and TL<sub>ad</sub> on Ru should be appropriate for the hydrogenation reaction. This is the reason the Ru(10)/KB cathode showed a high FE(MCH) in the electrohydrogenation of TL. As Ru/(Ru+Ir) decreased, catalytic hydrogenation activities decreased. Ir(10)/KB showed the lowest catalytic activity, which corresponds to a low FE(MCH) of Ir(10)/KB in the electrohydrogenation of TL. The TOF(Ru) values for the hydrogenation for Ru(10)/KB, Ru(8)-Ir(2)/KB, Ru(5)-Ir(5)/KB, and Ru(2)-Ir(8)/KB catalysts were similar ((2.9–4.6) × 10<sup>4</sup> h<sup>-1</sup>) and were not strongly dependent on Ru/(Ru+Ir). In addition, the app-TON(Ru) values were almost the same, ~2 × 10<sup>4</sup> h<sup>-1</sup> (Supporting Information). These indicated that catalytic hydrogenation proceeded on the Ru surface at the Ru(10)/KB, Ru(8)-Ir(2)/KB, Ru(5)-Ir(5)/KB, and Ru(2)-Ir(8)/KB catalysts and the surface nature of Ru on the Ru particle and that of Ru on the Ru-Ir alloy particle were similar. These facts strongly suggested that MCH should be formed by the reaction between H<sub>ad</sub> on Ru and TL<sub>ad</sub> on Ru in the electrohydrogenation reaction on the Ru(10)/KB, Ru(8)-Ir(2)/KB, Ru(5)-Ir(5)/KB, and Ru(2)-Ir(8)/KB cathodes.

On the basis of the above results, we conclude that electrohydrogenation of TL at the Ru-Ir alloy particle proceeded as follows (Figure 11): (i) H<sub>ad</sub> on Ir formed by the electrochemical reduction of H<sup>+</sup> (H<sup>+</sup> + e<sup>-</sup> + Ir → H<sub>ad</sub>-Ir),

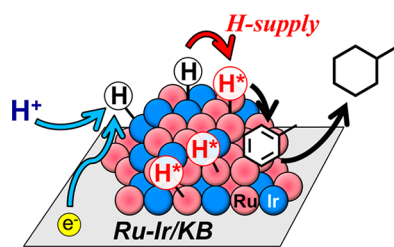


**Figure 11.** Reaction model for the electrohydrogenation of TL to MCH on a KB-supported Ru-Ir alloy cathode.

(ii)  $H_{ad}$  migrates from the Ir surface to the Ru surface ( $H_{ad}-Ir + Ru \rightarrow Ir + H_{ad}-Ru$ ), and (iii)  $H_{ad}$  on Ru reacted with  $TL_{ad}$  on Ru and as a result MCH is formed ( $6H_{ad}-Ru + TL_{ad}-Ru \rightarrow MCH + nRu$ ). Ir and Ru work as an  $H_{ad}$  formation electrocatalyst and a hydrogenation catalyst, respectively. The overpotential for the electrohydrogenation of TL at the Ru-Ir/KB cathode remarkably decreased to compare with that of Ru(10)/KB because formation of  $H_{ad}$  on Ru was accelerated by the addition of Ir. The slight decrease in FE(MCH) by the addition of Ir was due to formation of  $H_2$  by coupling of  $H_{ad}-Ir$  on a small Ir ensemble. A key factor of the unique nature of Ru and Ir would be a weak interaction between Ru and Ir in the Ru-Ir alloy, as observed in XPS spectra.

## CONCLUSION

We found the synergy of Ru and Ir for the electrohydrogenation of TL to MCH. The overpotential for the electrohydrogenation on Ru/KB decreased by the addition of Ir without a significant decrease in FE(MCH). Characterization studies using TEM-EDS, XRD, XAFS, XPS, and CV studies revealed that Ru and Ir formed an hcp-structured alloy in the Ru-Ir/KB electrocatalysts and that the electronic interaction between Ru and Ir in the Ru-Ir alloy is weak. The LSV studies for the hydrogen evolution and kinetic studies for the hydrogenation of TL indicated the collaboration of Ir electrocatalysis of  $H_{ad}$  formation and Ru catalysis of the hydrogenation of TL with  $H_{ad}$ . On the basis of the above results, an electrochemical spillover mechanism on the Ru-Ir alloy was proposed. In future work, we will tune the surface structure of the Ru-Ir alloy and develop more selective and active electrocatalysts for the electrohydrogenation of TL to MCH.

## ASSOCIATED CONTENT

### Supporting Information

The Supporting Information is available free of charge on the ACS Publications website at DOI: 10.1021/acscatal.8b03610.

Experimental details, XRD analysis, reagents and materials, TEM-EDS analysis, and EXAFS oscillations (PDF)

## AUTHOR INFORMATION

### Corresponding Author

\*E-mail for I.Y.: yamanaka.i.aa@m.titech.ac.jp.

### ORCID

Kiyotaka Asakura: 0000-0003-1077-5996

Ichiro Yamanaka: 0000-0002-9734-5659

### Notes

The authors declare no competing financial interest.

## ACKNOWLEDGMENTS

This work was financially supported by the Cross-ministerial Strategic Innovation Promotion Program (SIP), “energy-carrier” (funding agency: Council for Science, Technology and Innovation (CSTI)), and New Energy and Industrial Technology Development Organization (NEDO). XAFS measurements were performed at the Photon Factory and Photon Factory Advanced Ring of Institute for Materials Structures Science, High Energy Accelerator Research Organization (KEK-IMSS), Tsukuba, Japan, with the proposal number 2016G546. TEM-EDS measurements were supported by Ookayama Materials Analysis Division, Tokyo Institute of Technology.

## REFERENCES

- (1) Eberle, U.; Felderhoff, M.; Schüth, F. Chemical and Physical Solutions for Hydrogen Storage. *Angew. Chem., Int. Ed.* **2009**, *48*, 6608–6630.
- (2) (a) Gretz, J.; Baselt, J. P.; Ullmann, O.; Wendt, H. The 100 MW euro-Quebec hydro-hydrogen pilot project. *Int. J. Hydrogen Energy* **1990**, *15*, 419–424. (b) Gretz, J.; Drolet, B.; Kluyskens, D.; Sandmann, F.; Ullmann, O. Status of the hydro-hydrogen pilot project (EQHPP). *Int. J. Hydrogen Energy* **1994**, *19*, 169–174.
- (3) Okada, Y.; Sasaki, E.; Watanabe, E.; Hyodo, S.; Nishijima, H. Development of dehydrogenation catalyst for hydrogen generation in organic chemical hydride method. *Int. J. Hydrogen Energy* **2006**, *31*, 1348–1356.
- (4) Bourane, A.; Elanany, M.; Pham, T. V.; Katikaneni, S. P. An overview of organic liquid phase hydrogen carriers. *Int. J. Hydrogen Energy* **2016**, *41*, 23075–23091.
- (5) (a) Okada, Y. Large Scale  $H_2$  Storage and Transportation System by Organic Chemical Hydride Method. *J. Jpn. Inst. Energy* **2012**, *91*, 473–478. (b) Okada, Y.; Imagawa, K.; Kawai, N.; Mikuriya, T.; Yasui, M. Hydrogen Energy Storage and Transportation Technology for a Large-Scale: Organic Chemical Hydride Method “SPERA Hydrogen” System. *J. Jpn. Inst. Energy* **2014**, *93*, 15–20. (c) Chiyoda Corporation Demonstration of Massive  $H_2$  Energy Storage and Transportation System by Organic Chemical Hydride Method and  $H_2$  Supply Chain Concept. *J. Jpn. Inst. Energy* **2015**, *94*, 611–617.
- (6) (a) Langer, S. H.; Yurchak, S. Electrochemical Reduction of the Benzene Ring by Electrogenative Hydrogenation. *J. Electrochem. Soc.* **1969**, *116*, 1228–1229. (b) Langer, S. H.; Collucci-Rios, J. A. Chemicals with power—Instead of waste heat produce useful power from chemical reactions. *CHEMTECH* **1985**, *15*, 226–233.
- (7) (a) Otsuka, K.; Yamanaka, I. Electrochemical cells as reactors for selective oxygenation of hydrocarbons at low temperature. *Catal. Today* **1998**, *41*, 311–325. (b) Otsuka, K.; Yamanaka, I. Oxygenation of alkanes and aromatics by reductively activated oxygen during  $H_2$ – $O_2$  cell reactions. *Catal. Today* **2000**, *57*, 71–86. (c) Otsuka, K.; Yamanaka, I.; Hosokawa, K. A fuel cell for the partial oxidation of cyclohexane and aromatics at ambient temperatures. *Nature* **1990**, *345*, 697–698. (d) Yamanaka, I.; Murayama, T. Neutral  $H_2O_2$  Synthesis by Electrolysis of Water and  $O_2$ . *Angew. Chem., Int. Ed.* **2008**, *47*, 1900–1902. (e) Yamanaka, I.; Tazawa, S.; Murayama, T.; Ichihashi, R.; Hanaizumi, N. Catalytic Synthesis of Neutral  $H_2O_2$  Solutions from  $O_2$  and  $H_2$  by a Fuel Cell Reaction. *ChemSusChem* **2008**, *1*, 988–992. (f) Ogihara, H.; Maezuru, T.; Ogishima, Y.; Yamanaka, I. Electrochemical Reduction of  $CO_2$  to CO by a Co-N-C Electrocatalyst and PEM Reactor at Ambient Conditions. *ChemistrySelect* **2016**, *1*, 5533–5537.
- (8) Itoh, N.; Xu, W. C.; Hara, S.; Sakaki, K. Electrochemical coupling of benzene hydrogenation and water electrolysis. *Catal. Today* **2000**, *56*, 307–314.
- (9) Mitsushima, S.; Takakuwa, Y.; Nagasawa, K.; Sawaguchi, Y.; Kohno, Y.; Matsuzawa, K.; Awaludin, Z.; Kato, A.; Nishiki, Y. Membrane Electrolysis of Toluene Hydrogenation with Water

Decomposition for Energy Carrier Synthesis. *Electrocatalysis* **2016**, *7*, 127–131.

(10) (a) Nagai, K.; Nagasawa, K.; Mitsushima, S. OER Activity of Ir-Ta-Zr Composite Anode as a Counter Electrode for Electrohydrogenation of Toluene. *Electrocatalysis* **2016**, *7*, 441–444.

(b) Matsuoka, K.; Miyoshi, K.; Sato, Y. Electrochemical reduction of toluene to methylcyclohexane for use as an energy carrier. *J. Power Sources* **2017**, *343*, 156–160. (c) Nagasawa, K.; Sawaguchi, Y.; Kato, A.; Nishiki, Y.; Mitsushima, S. Rate-Determining Factor of the Performance for Toluene Electrohydrogenation Electrolyzer. *Electrocatalysis* **2017**, *8*, 164–169. (d) Nagasawa, K.; Kato, A.; Nishiki, Y.; Matsumura, Y.; Atobe, M.; Mitsushima, S. The effect of flow-field structure in toluene hydrogenation electrolyzer for energy carrier synthesis system. *Electrochim. Acta* **2017**, *246*, 459–465.

(11) Higuchi, E.; Ueda, Y.; Chiku, M.; Inoue, H. Electrochemical Hydrogenation Reaction of Toluene with Pt<sub>x</sub>Ru Alloy Catalysts-Loaded Gas Diffusion Electrodes. *Electrocatalysis* **2018**, *9*, 226–235.

(12) Takano, K.; Tatenno, H.; Matsumura, Y.; Fukazawa, A.; Kashiwagi, T.; Nakabayashi, K.; Nagasawa, K.; Mitsushima, S.; Atobe, M. Electrocatalytic Hydrogenation of Toluene Using a Proton Exchange Membrane Reactor. *Bull. Chem. Soc. Jpn.* **2016**, *89*, 1178–1183.

(13) Inami, Y.; Ogihara, H.; Yamanaka, I. Selective Electrohydrogenation of Toluene to Methylcyclohexane Using Carbon-Supported Non-Platinum Electrocatalysts in the Hydrogen Storage System. *ChemistrySelect* **2017**, *2*, 1939–1943.

(14) Inami, Y.; Ogihara, H.; Yamanaka, I. Effects of Carbon Supports on Ru Electrocatalysis for the Electrohydrogenation of Toluene to Methylcyclohexane. *Electrocatalysis* **2018**, *9*, 204–211.

(15) Rehr, J. J.; Albers, R. C.; Zabinsky, S. I. High-order multiple-scattering calculations of x-ray-absorption fine structure. *Phys. Rev. Lett.* **1992**, *69*, 3397–3400.

(16) Ohyama, J.; Kumada, D.; Satsuma, A. Improved hydrogen oxidation reaction under alkaline conditions by ruthenium–iridium alloyed nanoparticles. *J. Mater. Chem. A* **2016**, *4*, 15980–15985.

(17) Godoi, D. R. M.; Perez, J.; Villullas, H. M. Effects of Alloyed and Oxide Phases on Methanol Oxidation of Pt–Ru/CNnucatalysts of the Same Particle Size. *J. Phys. Chem. C* **2009**, *113*, 8518–8525.

(18) Chen, J.; Yao, C.; Zhao, Y.; Jia, P. Synthesis gas production from dry reforming of methane over Ce<sub>0.75</sub>Zr<sub>0.25</sub>O<sub>2</sub>-supported Ru catalysts. *Int. J. Hydrogen Energy* **2010**, *35*, 1630–1642.

(19) Kahl, J. M.; Poll, C. G.; Oropeza, F. E.; Ablett, J. M.; Céolin, D.; Rueff, J.-P.; Agrestini, S.; Utsumi, Y.; Tsuei, K. D.; Liao, Y. F.; Borgatti, F.; Panaccione, G.; Regoutz, A.; Egdel, R. G.; Morgan, B. J.; Scanlon, D. O.; Payne, D. J. Understanding the Electronic Structure of IrO<sub>2</sub> Using Hard-X-ray Photoelectron Spectroscopy and Density-Functional Theory. *Phys. Rev. Lett.* **2014**, *112*, 117601.

(20) Pauling, L. *The Nature of the Chemical Bond—An Introduction to Modern Structural Chemistry*, 3rd ed.; Cornell University Press: 1960.

(21) Pourbaix, M. *Atlas of Electrochemical Equilibrium in Aqueous Solutions*, 2nd ed.; NACE International: 1974.

(22) Ticanelli, E.; Beery, J. G.; Paffett, M. T.; Gottesfeld, S. An electrochemical, ellipsometric, and surface science investigation of the PtRu bulk alloy surface. *J. Electroanal. Chem. Interfacial Electrochem.* **1989**, *258*, 61–77.

(23) Senna, T.; Ikemiya, N.; Ito, M. In situ IRAS and STM of adsorbate structures on an Ir(111) electrode in sulfuric acid electrolyte. *J. Electroanal. Chem.* **2001**, *511*, 115–121.

(24) Furuya, N.; Koide, S. Hydrogen adsorption on iridium single-crystal surfaces. *Surf. Sci.* **1990**, *226*, 221–225.

(25) Conway, B. E.; Bai, L. Determination of adsorption of OPD H species in the cathodic hydrogen evolution reaction at Pt in relation to electrocatalysis. *J. Electroanal. Chem. Interfacial Electrochem.* **1986**, *198*, 149–175.

(26) Marković, N. M.; Grgur, B. N.; Ross, P. N. Temperature-Dependent Hydrogen Electrochemistry on Platinum Low-Index Single-Crystal Surfaces in Acid Solutions. *J. Phys. Chem. B* **1997**, *101*, 5405–5413.

(27) Durst, J.; Simon, C.; Hasché, F.; Gasteiger, H. A. Hydrogen Oxidation and Evolution Reaction Kinetics on Carbon Supported Pt, Ir, Rh, and Pd Electrocatalysts in Acidic Media. *J. Electrochem. Soc.* **2015**, *162*, F190–F203.

(28) Horiuti, J.; Polanyi, M. Exchange reactions of hydrogen on metallic catalysts. *Trans. Faraday Soc.* **1934**, *30*, 1164–1172.

(29) Polanyi, M.; Greenhalgh, R. K. Hydrogenation and atomic exchange of benzene. *Trans. Faraday Soc.* **1939**, *35*, 520–542.

(30) Burueva, D. B.; Salnikov, O. G.; Kovtunov, K. V.; Romanov, A. S.; Kovtunova, L. M.; Khudorozhkov, A. K.; Bukhtiyarov, A. V.; Prosvirin, I. P.; Bukhtiyarov, V. I.; Koptuyg, I. V. Hydrogenation of Unsaturated Six-Membered Cyclic Hydrocarbons Studied by the Parahydrogen-Induced Polarization Technique. *J. Phys. Chem. C* **2016**, *120*, 13541–13548.